Research Square

Preprints are preliminary reports that have not undergone peer review.
They should not be considered conclusive, used to inform clinical practice,
or referenced by the media as validated information.

Correlated Oxide Nanocrystal Inks for Hole-Selective Contacts in n-i-p Perovskite Photovoltaics

Shuai Yuan

shuaiy1991@g.ecc.u-tokyo.ac.jp

The University of Tokyo https://orcid.org/0000-0002-1390-3554

Congcong Zhang

the University of Tokyo https://orcid.org/0009-0000-9392-9342

Haruko Tamegai

the University of Tokyo

Miwako Furue

The University of Tokyo

Fumiyasu Awai

the University of Tokyo https://orcid.org/0000-0001-5091-4693

Takumi Kinoshita

The University of Tokyo

Satoshi Uchida

The University of Tokyo https://orcid.org/0000-0002-4971-574X

Takaya Kubo

The University of Tokyo

Hiroshi Segawa

The University of Tokyo

Article

Keywords:

Posted Date: August 31st, 2026

DOI: https://doi.org/10.21203/rs.3.rs-10067132/v1

License: This work is licensed under a Creative Commons Attribution 4.0 International License.
Read Full License

Additional Declarations: There is **NO** Competing Interest.

Abstract

NiO is one of the few wide-bandgap inorganic semiconductors exhibiting intrinsic p-type conduction, making it indispensable for optoelectronic applications. The emergence of aqueous colloidal dispersions of NiO_x nanocrystals underpins the most efficient p-i-n perovskite solar cells; however, their processing is typically restricted to water, limiting their use as hole-transporting layers atop perovskite absorbers in n-i-p architectures. Here, we develop nonpolar conductive NiO_x nanocrystal inks via a two-step ligand-exchange strategy that transfers the nanocrystals from aqueous to nonpolar media while regulating their colloidal and electronic properties. This technique enables ink-processable, doping-free, hole-selective contacts for efficient n-i-p perovskite solar cells, delivering performance exceeding that of Spiro-OMeTAD-based devices.

Introduction

Wide-bandgap p-type semiconductors compatible with low-temperature solution processing are essential for next-generation optoelectronic technologies[1, 2]. From this perspective, organic semiconductors have been successful due to the delocalization of lone-pair p_z electrons of heteroatoms into π-conjugation, which raises the highest occupied molecular orbital (HOMO) level and enables p-type character [3, 4]. In contrast, achieving hole-majority conduction in their wide-bandgap inorganic counterparts has been a longstanding challenge since early studies of GaN and ZnO[5, 6]. The difficulty is rooted in their deep valence band maximum (VBM) dominated by N and O 2*p* orbitals, which makes p-type doping inefficient.

Late transition-metal oxides such as NiO provide a rare exception. The high-energy Ni 3*d* orbital elevates its VBM and thus activates shallow acceptors, enabling p-type conductivity[7, 8]. However, unlike main-group metal oxides, the on-site Coulomb repulsion of partially filled 3*d* electrons must be taken into account. On the one hand, it splits the *d* manifold into occupied and unoccupied Hubbard bands, opening a Mott gap (Fig. 1a)[9–13]; otherwise, NiO would be metallic because the Fermi level lies within an open-shell *d* band. On the other hand, this strong Coulomb potential gives rise to electron correlation effects (**Supplementary Note 1**), generating many-body eigenstates that lie beyond the one-electron approximation[14–16]. At the experimental level, photoelectron spectroscopy (PES) does not directly reflect the occupied density of states but probes the many-body *N*-1 final states within the Sudden approximation[17–19]. As a result, the valence band structure and ensuing hole-transport mechanisms of NiO remain debated theoretically and experimentally, hindering its electronic tunability for semiconductor applications.

Apart from challenges in condensed-matter understanding, limitations in film deposition techniques also impede the widespread adoption of NiO. From a solution-processing perspective, thermal-decomposition sol-gel spin coating has been used for almost two decades[20–22]. Although this method is simple and low-cost, the high annealing temperature reaching 300°C required to form the NiO film hinders its

compatibility with other materials in device fabrication. The emergence of aqueous colloidal dispersions of NiO_x nanocrystals (NCs), pioneered by Jiang et al., offers an alternative route for low-temperature processing[23], and has been widely adopted as the hole-transporting layer in the most efficient p-i-n perovskite solar cells[24, 25]. However, the colloidal behavior and ink processibility of such NiO_x NCs remain unexplored. As a result, their processing is confined to aqueous media, hampering their integration as hole-selective contacts atop perovskite absorbers in n-i-p architectures. Overcoming this processing bottleneck would enable NiO_x NCs to serve a robust inorganic alternative to dopant-dependent Spiro-OMeTAD, which suffers from costly synthesis, dopant-induced ion migration, and post-treatment requirements.

In this work, we elucidate the electronic structure and colloidal properties of NiO_x NCs, and leverage these insights to develop nonpolar, conductive NiO_x NC inks that function as efficient hole-selective contacts in n-i-p perovskite solar cells. We first assess the valence band structure of NiO_x NCs through a photoemission study in combination with the band-edge transition selection rule, revealing Ni 3*d*-O 2*p* hybridization. We then functionalize aqueous NiO_x NC dispersion through a two-step ligand exchange, in which the protonated surface of aqueous NiO_x NCs provides binding sites for functional phosphonic acid ligands, endowing ligand-assisted phase transfer into nonpolar solvents. By tailoring functional moieties of ligands, the electronic coupling and dispersion of NiO_x NCs can be regulated, yielding ink-processable, doping-free hole-selective contacts for n-i-p perovskite photovoltaics. Devices incorporating NiO_x NC inks achieve a champion power conversion efficiency of 25.8% with damp-heat stability surpassing that of Spiro-OMeTAD-based counterparts. This technique establishes an alternative inorganic colloidal nanocrystal hole-transporting platform for perovskite photovoltaics.

Results

Electronic structure of NiO_x nanocrystals

NiO_x NCs, synthesized via chemical precipitation[23], adopt a rock-salt cubic phase composed of NiO_6 octahedra with O_h symmetry (Fig. 1b). This centrosymmetric point group underlies the crystal-field splitting (10*Dq*) and governs the electric-dipole selection rule for interband transition[26, 27]. To clarify the valence band structure of NiO_x NCs, we performed ultraviolet photoelectron spectroscopy (UPS, 21.2 eV) on a series of metal oxides with different *d*-electron configurations (Fig. 1c). d^{10} oxides such as SnO_2 and ZnO, as well as d^0 oxides such as TiO_2 show distinct O 2*p*-dominated VBMs at ~ 7 eV below vacuum. In contrast, NiO_x NC ($3d^8$) and CuO ($3d^9$) feature much shallower VBMs at ~ 5 eV dominated by open-shell 3*d* orbitals. Their O 2*p* peaks instead appear at higher binding energies ~ 9.5 eV, which points to *d-p* hybridization that forms deep bonding states (**Supplementary Note 2**)[28].

To further verify the 3*d* contribution in the valence band of NiO_x NCs, we performed valence-band X-ray photoelectron spectroscopy (XPS); meanwhile, a low-energy inverse photoelectron spectroscopy (LEIPS)

was conducted to capture the unoccupied states above the Fermi level (Fig. 1d). Below the Fermi level, NiO_x NCs exhibit a double-peaked 3*d* ($3d^8L^{-1}$) final state due to multiplet effects[29–32]. Above it, the Coulomb repulsion pushes the $3d^9$ states to higher energies (**Supplementary Fig. 1**)[9, 10, 13], forming a conduction band that emerges at 1.5 eV below vacuum. The combined PES and LEIPES measurements derive a bandgap of ~ 3.5 eV. This aligns well with the absorption spectrum (Fig. 1e), where the strong oscillator strength starts at ~ 355 nm (3.5 eV).

Such an intense band-edge electric-dipole transition further supports *d-p* hybridization at the VBM. The *d-p* antibonding states introduce the odd-parity contribution from the O 2*p* into the *d*-like VBM, so that it relaxes the parity-forbidden band-edge two-ion *d-d* transition and produces a non-zero transition dipole moment (Fig. 1f, **Supplementary Note 2**)[27, 28]. Beyond this optical effect, the hybridization of O 2*p* in the VBM is expected to favor hole delocalization because O 2*p* states are less correlated and support larger intersite hopping than localized Ni 3*d* [33]. This explains why NiO_x NC films can retain moderate hole mobility ~ 10^{-3} $cm^2V^{-1}s^{-1}$[34], despite their large hole effective mass being derived from angle-resolved photoemission spectroscopy (ARPES)[18, 19]. This makes NiO_x NCs a promising hole-transport material.

Two-step ligand exchange enabling phase-transferred NiO nanocrystal in nonpolar colloidal inks

Having understood the electronic structure, we next turned to regulating the colloidal behavior of NiO_x NCs. We developed a two-step ligand-exchange strategy to functionalize aqueous NiO_x NC dispersions (Fig. 2a). In aqueous media, the dispersibility of metal oxide nanoparticles is governed by the (de)protonation of surface hydroxyl groups, which defines the surface charge and thus establishes both the electrical double layer and hydration layers at the nanoparticle interface[36–38]. These interfacial structures provide interparticle repulsion, thereby stabilizing primary nanoparticles in water[36].

To probe the protonation behavior of surface hydroxyls on NiO_x NCs in water, we measured the pH-dependent zeta potential (Fig. 2b). The zeta potential remains positive over the pH range of 4–9, indicating that the surface hydroxyls are predominantly protonated under neutral conditions. This surficial structure modulates the interfacial hydrogen-bonding network of surrounding water molecules, as detected by Raman spectroscopy (Fig. 2c). With increasing NiO_x NC concentration, the ~ 3270 cm^{-1} O-H stretching band associated with tetrahedrally hydrogen-bonded double-donor double-acceptor (DDAA) water gradually decreases (**Supplementary Fig. 2**). In contrast, the higher-frequency bands assigned to less-coordinated donor-acceptor (DA) and double-donor-acceptor (DDA) configurations become more pronounced.

Given the protonated surface of NiO_x NCs in water, we reasoned that hydrogen-bond acceptor ligands could interact with surface proton-donating sites, thereby regulating NC aggregation and redispersion

(Fig. 2a). As the first step, we introduced acetonitrile (ACN), a water-miscible polar aprotic molecule whose nitrile N atom serves as a hydrogen-bond acceptor.

At a low ACN fraction, the NiO_x NCs remain dispersed in the ACN/H_2O mixture, enabling ACN-NiO_x surface interactions to be probed via the C ≡ N stretching vibration (v_2; Fig. 2d). At the fixed ACN/H_2O composition, increasing the NiO_x NC concentration induces a systematic blue shift and pronounced broadening of v_2 (Fig. 2e, f), supporting hydrogen bonding between the nitrile N of ACN and protonated sites on the NiO_x NC surface[42, 43]. At higher ACN fractions, increased ACN adsorption disrupts the interfacial hydration layer and exposes the methyl groups to the surface, thereby promoting NiO_x NC flocculation and separation from the dispersion medium (**Supplementary Fig. 3**).

In the second step, precipitated NCs were redispersed in chloroform (CF) solutions containing functional phosphonic acid ligands (Fig. 2a). During this ligand exchange, functional phosphonic acid ligands with polar headgroups further replace surface-bound ACN molecules, while the bulky organic side groups extend into the surrounding solvent to provide steric stabilization, thereby rendering the phase-transferred NCs dispersible in nonpolar media. Because paramagnetic Ni^{2+} centers limit nuclear magnetic resonance characterization, we instead use vibrational spectroscopy to probe the NiO_x NC/ligand interfacial structure. Among the phosphonic acid ligands examined, tert-butylphosphonic acid (*t*-BPA) exhibits detectable vibrational modes for each of the P-O, P = O, and O-H moieties in its phosphonic acid headgroup (**Supplementary Fig. 4**), making it a suitable model ligand for probing binding interactions at the NiO_x NC surface.

Polarization-dependent Raman spectroscopy of *t*-BPA crystals was employed to establish reliable assignments of these phosphonic-acid vibrations (Fig. 2g), providing a spectral benchmark to track their evolution across different molecular environments (Fig. 2h). Comparing free *t*-BPA in its monomeric state (**Supplementary Fig. 5**) with the NiO_x NC-bound state in solution, the O-H stretching band of the phosphonic acid headgroup at 2850–3000 cm^{-1}, as well as the C-C and C-H vibrations remains essentially unchanged (**Supplementary Fig. 6**). Notably, P-O and P = O stretching modes (900–1300 cm^{-1}) undergo pronounced shifts upon binding, indicating that surface anchoring primarily perturbs the P-O and P = O moieties. The *t*-BPA in the solid NiO_x/*t*-BPA sample retains predominantly bound-state features, with minor free-*t*-BPA-like contributions, suggesting limited ligand detachment upon solidification.

To further dissect the respective roles of the P-O and P = O moieties in surface binding, we compared ligands containing either moiety individually with those containing both (Fig. 2i, upper panel). Tributylphosphine oxide (TBPO) and tributyl phosphite (TBuP) serve as single-moiety ligands, bearing P = O and P-O moieties, respectively. In comparison, diethyl *n*-butane phosphonate (DEBP) and *n*-butylphosphonic acid (*n*-BPA) contain both. Only DEBP and *n*-BPA render the NiO_x NCs dispersible in CF, as evidenced by the pronounced NiO_x NC absorption (Fig. 2i, lower panel), indicating that effective surface anchoring likely requires both moieties. Moreover, this ligand-induced dispersibility is observed

only for protonated and deuterated NiO_x NCs (Fig. 2i and **Supplementary Fig. 7**). In contrast, the corresponding unprotonated NCs remain nondispersible (Fig. 2i and **Supplementary Fig. 8**). Together, these findings support a predominant multidentate binding of phosphonic acid ligands to protonated sites on the NiO_x NC surface through their P-O and P = O moieties.

Based on the aforementioned NiO_x NC/ligand binding configurations, we propose the mechanisms of a two-step ligand exchange for NiO_x NC phase transfer in Fig. 3a. To verify the ligand-exchanged NiO_x NCs, we characterized nonpolar inks by TEM and STEM (Fig. 3b). Elemental mapping shows phosphonic-acid-capped NiO_x NCs with sizes of ~ 5 nm. UV-vis spectroscopy provides further evidence of ligand attachment (Fig. 3c). Using [2-(3,6-dimethoxy-9H-carbazol-9-yl)ethyl]phosphonic acid (MeO-2PACz) ligand molecule as an example, the nonpolar NiO_x NC/ MeO-2PACz ink exhibits the characteristic UV absorption from the vibronic fine structure of carbazole chromophores, arising from the π-π* singlet transition. This signal remains nearly unchanged after four rinsing cycles, indicating stable binding.

The colloidal dispersibility is strongly ligand-dependent (Fig. 3d). Alkyl ligands such as *n*-BPA and *t*-BPA allow dispersion in CF. In comparison, conjugated aromatic-amine ligands provide even stronger stabilization in aromatic solvents (chlorobenzene, CB). MeO-2PACz- and (4-(bis(4-methoxyphenyl)amino)benzyl)phosphonic acid (MeO-TPA-PA) -capped NiO_x NCs show high solubility and remain stable for one month (Fig. 3e and **Supplementary Fig. 9**), whereas *n*-BPA-, *t*-BPA-, and 2PACz-capped NCs exhibit poorer stability due to the limitation of van der Waals-driven aggregation, lower steric protection, or π-stacking, respectively.

NiO nanocrystal films processed by nonpolar colloidal inks

Having elucidated the colloidal engineering of NiO_x NCs, we next explore how ligand design affects film-level electrical properties. We tailored the phosphonic acid ligands with carbazole (2PACz), 3,6-dimethoxycarbazole (MeO-2PACz), and 4,4'-dimethoxytriphenylamine (MeO-TPA-PA) functional groups (Fig. 4a). Here, methoxy substitution increases electron density and raises the HOMO of p-type moieties, while the triphenylamine unit, lacking the rigid fused-ring structure of carbazole, is more electron-donating and therefore exhibits an even higher HOMO level.

This ligand series offers a stepwise HOMO-level ladder for tuning the energetic alignment between the ligand shell and the VBM of the NiO_x NC core, as confirmed by UPS measurements (Fig. 4a and **Supplementary Fig. 10**). NiO_x NCs capped with *t*-BPA and 2PACz show deep VBM levels of 5.23 and 5.42 eV, respectively, with 2PACz lying 0.4 eV deeper than the ligand-free NiO_x NC. By contrast, more electron-rich MeO-2PACz and MeO-TPA-PA ligands bring much smaller offsets within 0.1 eV. The energetic alignment between ligands and nanocrystal core determines interparticle hole hopping within stacked nanocrystal films (Fig. 4b). In hole-only devices (ITO/NiO_x NCs/Au), the capping of MeO-2PACz and MeO-TPA-PA ligands retains the conductivity of NiO_x NC films at levels comparable to doped Spiro-OMeTAD,

while insulating ligands or ligands with large energetic offsets introduce severe electrical losses (Fig. 4c).

Before incorporating nonpolar NiO_x NC inks as hole-selective contacts in n-i-p perovskite solar cells, we assessed their film processability onto perovskite films. Top-view and cross-sectional scanning electron microscopy (SEM) images show dense, uniform NiO_x NC overlayers on perovskite, regardless of the ligand used (Fig. 4d), validating the good compatibility.

We next studied carrier dynamics in perovskite/NiO_x NCs bilayers using femtosecond pump-probe and nanosecond time-resolved photoluminescence (TRPL) spectroscopies to track photoexcitation from hot-carrier thermalization and band-edge relaxation to recombination across different timescales. Because deep traps in perovskites can directly capture hot carriers and thereby accelerate their cooling[44], we first performed interband transient absorption (TA) measurements using a 480 nm pump to excite hot carriers, while maintaining low excitation densities to avoid side effects of the hot-phonon bottleneck and Auger reheating[45]. The cooling dynamics over 1–20 ps show no significant variation over different bilayers (**Supplementary Fig. 11**), suggesting that NiO_x NCs coating does not introduce a detectable density of fast hot-carrier-capturing interfacial deep traps. Following hot carrier cooling, the band-edge decay kinetics of all samples remain nearly identical within 1 ns, consistent with TA measurements under band-edge excitation using a 700 nm pump (Fig. 4e and **Supplementary Fig. 11**). At longer timescales, TRPL reveals reduced carrier lifetimes in all perovskite/hole-selective contact bilayers (Fig. 4f), owing to hole extraction. NiO_x NC/MeO-2PACz and NiO_x NC/MeO-TPA-PA shorten the average perovskite lifetimes from 320 ns to ~ 110 ns, which is comparable to that of the perovskite/Spiro-OMeTAD. Consistent with this, photoluminescence quantum yield (PLQY) measurements show similar nonradiative quenching in perovskite/NiO_x NCs and perovskite/Spiro-OMeTAD bilayers (Fig. 4g).

Nonpolar ink-processable NiO_x nanocrystal films for hole-selective contacts in n-i-p perovskite solar cells

We integrated nonpolar ink-processable NiO_x NC films into n-i-p perovskite solar cells as hole-selective contacts, while SnO_2 NC films serve as electron-transporting layers. The entire device structure is visualized using cross-sectional TEM and STEM (Fig. 5a and **b**). NiO_x NC film measuring ~ 50 nm atop the perovskite absorber is uniform, and each functional layer matches well with the elemental mappings. Devices constructed by NiO_x NC/MeO-2PACz and NiO_x NC/MeO-TPA-PA films yield the champion power conversion efficiencies (PCE) of 24.9% and 25.8% (Fig. 5c and **Supplementary Fig. 12**), respectively, corresponding to the short-circuit current density (J_{sc}) of 25.4 mA/cm^2 and 25.8 mA/cm^2, the open-circuit voltage (V_{oc}) of 1.173 V and 1.186 V, and the fill factor (*FF*) of 83.6% and 84.5%. Notably, the champion NiO_x NC/MeO-TPA-PA device outperforms the Spiro-OMeTAD reference device, which exhibits a J_{sc} of 25.9 mA/cm^2, a V_{oc} of 1.181 V, an *FF* of 82.5%, and a PCE of 25.2%. For each device, their integrated photocurrents derived from incident photon-to-current efficiency (IPCE) spectra agree well

with the J_{sc} obtained from *J-V* measurements (Fig. 5d). NiO_x NCs functionalized with *n*-BPA, *t*-BPA, and 2PACz ligands exhibit inferior PCE, limited by poor V_{oc} and *FF*. Compared with NiO_x NC/MeO-TPA-PA and Spiro-OMeTAD, NiO_x NC/MeO-2PACz devices exhibit poorer reproducibility, as evidenced by a broader average PCE distribution across 21 single cells fabricated from different batches (Fig. 5e and **Supplementary Fig. 13**), likely due to the more sensitive ink processability, which influences nanocrystal stacking.

Operational stability was evaluated by maximum power point (MPP) tracking under 1-sun illumination at a controlled temperature of 25 ± 2°C in dry air (ISOS-L1) using unencapsulated devices (Fig. 5f). NiO_x NC/MeO-2PACz devices exhibit the best operational stability, retaining 97% of their initial PCE after 1800 s. The long-term stability of encapsulated devices was further assessed under industry-relevant damp-heat conditions (85°C and 85% relative humidity). Under these conditions, n-i-p devices employing NiO_x NC colloidal inks exhibited substantially better stability than their Spiro-OMeTAD-based counterparts (Fig. 5g and **Supplementary Fig. 14**). After 312 h of damp-heat aging, the NiO_x/MeO-2PACz and NiO_x/MeO-TPA-PA devices retained, on average, 91.5% and 83.8% of their initial PCEs, respectively. We attribute the comparatively weaker stability of NiO_x/MeO-TPA-PA devices to redox interactions between the NiO_x NC core and the MeO-TPA-PA ligand **(Supplementary Fig. 15**), where the formation of radical cations may perturb the energetic alignment and electronic properties of this hole-transporting layer, as well as the perovskite/HTL interface during device operation[46]. These results highlight the importance and the potential of ligand design for further optimizing device performance in this technique.

Discussion

In conclusion, we established a two-step ligand-exchange strategy in which hydrogen-bond-accepting ligands interact with protonated hydroxyl groups on aqueous NiO_x NCs, enabling their phase transfer from water to nonpolar solvents. This strategy concurrently regulates colloidal dispersion, work function, and interparticle electronic coupling, producing nonpolar NiO_x NC colloidal inks that function as doping-free, effective hole-transport layers for n-i-p perovskite solar cells. The optimized devices achieve a power conversion efficiency of 25.8%, outperforming that of Spiro-OMeTAD counterparts. This work establishes a practical route toward low-temperature, solvent-processable, wide-bandgap p-type inorganic semiconductor inks for optoelectronic applications

Experimental Section

Materials and Chemicals.

$Ni(NO_3)_2{\cdot}6H_2O$ (nickel(II) nitrate hexahydrate), NaOH (sodium hydroxide), 4-(bis(4-methoxyphenyl)amino)benzaldehyde, I_2 (elemental iodine), triethyl phosphite, bromotrimethylsilane (TMSBr), methanol, IPA (2-propanol), FAI (formamidinium iodide) (> 99%), PbI_2 (lead iodide) (99.99%), RbI (rubidium iodide) and OAI (n-octylammonium iodide), tributylphosphine oxide (TBPO), tributyl phosphite

(TBuP) and *n*-butanephosphonate (DEBP) were purchased from TCI (Tokyo Chemical Industry) Co., Ltd. MACl (methylammonium chloride) was purchased from FUJIFILM Wako Pure Chemical Corporation. Anhydrous DMF (N, N-dimethylformamide) (≥ 99.9%), DMSO (dimethyl sulfoxide) (≥ 99.9%), ACN (acetonitrile), CB (chlorobenzene), HEX (n-hexane), CF (chloroform), anisole, LiF (lithium fluoride) (≥ 99.99%), MeO-2PACz (> 98.0%), 2PACz, *n*-butylphosphonic acid (*n*-BPA), tert-butylphosphonic acid (*t*-BPA) Spiro-MeOTAD, LiTFSI (lithium bis(trifluoromethanesulfonyl)imide), and TBP (4-tert-butylpyridine) were purchased from Sigma-Aldrich. Au (gold) (99.999%) was purchased from Kojundo Chemical Laboratory Co.

Preparation of NiO nanocrystals and nonpolar inks

The synthesis of NiO_x NC powder was performed as follows: 10 g of $Ni(NO_3)_2 \cdot 6H_2O$ was dissolved in 50 mL of deionized water under magnetic stirring. A 10 M NaOH solution was then added dropwise through a pressure-equalizing dropping funnel until the pH reached 10. The resulting turbid green suspension was collected by centrifugation, and the precipitate was washed twice with deionized water. The washed precipitate was subsequently frozen at -18°C for 2 h, followed by another centrifugation and dried in a vacuum overnight. Finally, the obtained powder was annealed in an oven at 270°C for 1.5 h.

To prepare the nonpolar inks, the NiO_x NC powder was first dispersed in water at a concentration of 20 mg/mL. ACN was then added to induce NC precipitation. After removal of the supernatant, the precipitate was used in the subsequent steps. The phosphonic acid ligands were separately dissolved in CF to form ligand solutions, with ligand concentrations ranging from 3 to 5 mg/mL for every 5 mg of NCs. For 2PACz and MeO-2PACz, a small amount of EtOH was mixed into CF to improve the solubility. The ligand solution was then mixed with the precipitated NCs at an NC concentration of 5 mg/mL. After ligand grafting by vortex mixing for 2 min, methanol was added as an antisolvent to precipitate the NCs and remove excess ligands, and this washing step was repeated twice. The supernatant was discarded, and the resulting NC precipitates were redispersed in a nonpolar solvent, such as CF, CB, or anisole, depending on the ligand used in the previous step. The synthesis of the MeO-TPA-PA molecule can be found in the supporting information.

The fabrication of n-i-p perovskite solar cells

The fluorine-doped tin oxide (FTO) substrates underwent a thorough cleaning process, beginning with 20 min ultrasonic baths in acetone and isopropanol, respectively. This was followed by a 30 min UV-O^3 cleaning treatment. For the electron transport layers (ETLs), a solution containing 5 wt% SnO_2 and 0.5 wt% KCl in deionized water was spin-coated on the FTO substrates at 4000 rpm for 30 s. This layer was then annealed at 160°C for 30 min. The perovskite precursor solution was prepared by dissolving 0.691 g of PbI_2 in the mixture of 900 µL DMF and 100 µL DMSO. Another solution for the FAI-IPA precursor involved dissolving 0.095 g of FAI and 0.013 g of MACl in 1000 µL IPA. The perovskite layers were

deposited in a two-step process, starting with the PbI_2-DMF solution spin-coated at 2000 rpm for 30 s, followed by a short 70°C annealing for 1 min. The FAI-IPA solution was then applied over the PbI_2-DMF layer at 3000 rpm for 30 s, with a subsequent thermal treatment at 140°C for 15 min.

For the hole-transport material (HTM), NiO_x NC nonpolar inks functionalized with various ligands were used at a concentration of 30 mg/mL and spin-coated directly onto the perovskite layers at 3000 rpm, without any post-deposition baking or aging treatment. For the control HTM, a Spiro-OMeTAD solution was prepared by dissolving 0.162 g of Spiro-OMeTAD in chlorobenzene, followed by the addition of 39.4 µL of Li-TFSI solution (130 mg Li-TFSI dissolved in 250 µL acetonitrile) and 94.5 µL of tBP. The HTM solution was spin-coated onto the perovskite layer at 4000 rpm for 30 s. The resulting samples were then exposed to dry ambient air for varying durations to promote oxidation. Subsequently, a 100 nm thick Au electrode was deposited by thermal evaporation under high vacuum (5×10^{-4} Pa), yielding devices with an active area of 0.18 cm^2.

TEM and STEM measurements

TEM and STEM images of the samples were acquired using a high-resolution scanning transmission electron microscope (HR-STEM; HF5000, Hitachi High-Tech, Japan) operated at an accelerating voltage of 200 kV. TEM observations were performed using a probe current of 3734 pA, a condenser aperture diameter of 300 µm, and an objective aperture diameter of 50 µm. Images were acquired using a Gatan Rio16 CMOS camera. Image acquisition and EDX analysis were controlled using the Digital Micrograph software (Gatan Inc.), which was used to acquire TEM and STEM images as well as to perform and process EDX mapping. HAADF-STEM observations were conducted using a probe current of 229 pA and a STEM condenser aperture diameter of 35 µm.

EDS analyses were carried out using an EDAX Elite T Ultra Model 1171 STEM-EDS silicon drift detector (SDD) with a detection area of 160 mm². The EDS elemental mapping shown in Fig. 2e was performed at a magnification of 400,000× with a pixel dwell time of 0.005 s, 10 passes (frames), and an image resolution of 120 × 120 pixels.

The step size was 2.3 Å. Drift correction was applied after each frame acquisition, resulting in a total acquisition time of approximately 14.3 min. The EDS elemental mapping shown in Fig. 4b was performed at a magnification of 20,000× with a pixel dwell time of 0.01 s, 10 passes (frames), and an image resolution of 74 × 72 pixels. The step size was 10 nm. Drift correction was applied after each frame acquisition, resulting in a total acquisition time of approximately 10.7 min. Cross-sectional TEM specimens were prepared using a Hitachi High-Tech NX5000 focused ion beam (FIB) system.

Photoelectron and low-energy inverse photoelectron spectroscopies

The valence band structure, elemental analysis, and energy-level alignment at the interfaces were comprehensively characterized by a combination of UPS and XPS. UPS and XPS measurements were

performed using a Kratos AXIS ULTRA HAS system. For UPS, He I_α radiation (photon energy = 21.22 eV) was used as the excitation source to probe the valence electronic structure, while XPS employed a monochromatic Al K_α source (photon energy = 1486.6 eV) to analyze core-level binding energies and elemental composition. To ensure the accuracy of the energy scale, the binding energy values obtained from UPS and XPS were calibrated using standard reference measurements. Specifically, the Fermi edge was aligned to 0 eV using a clean gold (Au) surface for UPS, while the Au $4f_{7/2}$ core-level peak was set to 84.0 eV for XPS calibration. Complementary information about the unoccupied states and conduction band alignment was obtained from LEIPES measurements, which were conducted using a system provided by ALS Technology Co., Ltd. These measurements were carried out under ultrahigh vacuum conditions, with a base pressure maintained at approximately 1.0×10^{-10} Torr. Such stringent vacuum conditions are critical for minimizing surface contamination and preserving the intrinsic electronic properties of the samples during data acquisition.

PL, TRPL, Raman and IR spectra measurements

PL spectra were recorded using a high-sensitivity JASCO FP-8700 Spectrofluorometer, enabling accurate assessment of emission characteristics across a wide spectral range. PLQY spectra were obtained using a UV-NIR absolute spectrometer (model C13534, Hamamatsu Photonics K.K.), which allows for direct and reliable measurement of quantum efficiency from ultraviolet to near-infrared regions. Spatially resolved PL mapping, Raman and TRPL spectra were collected using the Nanofinder®30 system from Tokyo Instruments, Inc. All PL-based measurements were conducted under excitation with a 532 nm laser source, which was chosen to match the absorption characteristics of the samples under investigation. IR absorption spectra measured in either transmittance or attenuated total reflection (ATR) modes were conducted using a SHIMADZU AIMsight™ FTIR spectrometer with a ZnSe crystal.

Ultraviolet-visible absorption spectrophotometry

Spectra were recorded using a Shimadzu ultraviolet-visible-near infrared spectrophotometer (UV-3600Plus). The absorption spectra were measured on nanocrystal thin films

Zeta potential measurements

The Zeta potentials of the NiO_x aqueous suspensions under various ionic strengths were measured using a ZetaSizer Nano ZS. The net electrophoretic mobility of particles was measured, which is converted to its zeta potential by Henry's approximation

Transient absorption spectroscopy (TAS) measurements

All sample films were prepared in the same way as in devices with encapsulation. The output of a Ti: sapphire amplifier system (Spectra Physics Solstice Ace) operated at 1 kHz and generating ~ 90-fs pulses was split into pump and probe beams. The 480 nm and 700 nm pump pulses were created using an optical parametric amplifier (OPA, Spectra Physics TOPAS-C Light Conversion 80C0) while modulated by a chopper. A mechanical delay stage (Thorlabs DDS300-E/M) was used to regulate the probe beam before being focused onto a sapphire crystal, which gives rise to the while-light filamentation, creating

the supercontinuum white probe beam covering 500–900 nm. The transmitted signals were collected with a monochrome line scan camera composed of silicon double arrays (SOLAR TII MS2004i spectrometer).

Device photovoltaic properties measurement

Current density-voltage (*J-V*) characteristics of the devices were measured under standard simulated solar illumination (AM 1.5G, 100 mW cm^{-2}, equivalent to 1 sun) using a 450 W xenon lamp solar simulator (model YSS-80A, Yamashita Denso Co., Ltd., Japan). Prior to measurement, the light intensity was carefully calibrated using a certified silicon photodiode reference cell to ensure the accuracy of the 1 sun illumination condition. To define the active area of the device precisely and eliminate contributions from edge leakage or overestimation due to the non-uniform device edges, a metal optical mask with an aperture area of 0.18 cm^2 was employed. The *J-V* measurements were conducted in both reverse and forward scan directions to evaluate hysteresis behavior. The reverse scan was initiated from + 1.2 V to -0.2 V, followed by a forward scan from − 0.2 V to + 1.2 V, each performed at a constant voltage sweep rate of 50 mV s^{-1}. All measurements were conducted under controlled dry-air conditions, with a maintained relative humidity level below 500 ppm, to ensure the environmental stability of the device and reduce the influence of moisture on photovoltaic performance. MPPT analysis was also carried out under the same conditions to assess the stabilized output of the devices over time. A damp-heat aging test was performed using the SH-642 bench-top type temperature and humidity chamber (ESPEC; **Supplementary Fig. 16**). IPCE spectrum was measured using a solar simulator system (model CEP-2000BX, Bunko-Keiki Co., Ltd.). The spectral response system was calibrated using a standard silicon reference solar cell to ensure accurate measurement of photocurrent as a function of wavelength.

DFT calculations

First-principles calculations based on DFT were performed using the Vienna Ab initio Simulation Package (VASP) [47, 48]. The generalized gradient approximation (GGA) in the form proposed by Perdew, Burke, and Ernzerhof (PBE) [49] was employed for the exchange-correlation functional. The interaction between ionic cores and valence electrons was described using the projector-augmented wave (PAW) method [50, 51]. The Kohn–Sham wave functions were expanded in a plane-wave basis set with a kinetic-energy cutoff of 450 eV. Electronic partial occupancies were treated using the Gaussian smearing method with a smearing width of 0.05 eV. Both atomic positions and lattice parameters were fully relaxed until the maximum residual force on each atom was below 0.05 eV $Å^{-1}$. Owing to the large dimensions of the simulation supercell, the Brillouin zone was sampled using a Γ-centered 1×1×1 k-point mesh [52]. The electronic self-consistent-field iterations were considered converged when the total-energy difference between successive steps was below 10^{-5} eV. Long-range van der Waals interactions, which are important for accurately describing physisorption, were included using the Grimme DFT-D3 dispersion correction [53, 54]. For the NiO_x systems, spin-polarized calculations were performed with an antiferromagnetic configuration adopted for the NiO_x. The density of states (DOS) was evaluated using

the tetrahedron method with Blöchl corrections. The energy range was discretized using 1000 grid points, and the atom- and orbital-projected DOS was obtained through PAW-based projections.

Declarations

Competing Interest

The authors declare no competing interests.

Author contributions

The project was conceived and designed by S. Y. and H. S. S. Y. synthesized NiO_x nanocrystals, ligand crystals and ligand molecules, and regulated the NiO_x colloidal inks, while conducting PES, IPES, femtosecond pump-probe, TRPL, PL, PLQY, XRD, Raman and IR spectra, as well as the colloidal characteristics, and established the Hamiltonian for the tight-binding approximation, also demonstrating the radical reactions. C. C. Z. fabricated the perovskite solar cells, performed the IV, IPCE, as well as the stability measurements, and carried out the DFT + *U* theoretical calculations. T. H. conducted FIB, STEM and TEM measurements. S. Y. wrote the manuscript. All authors discussed the results and commented on the manuscript.

Acknowledgments

This work is supported by the New Energy and Industrial Technology Development Organization (NEDO, Japan).

Data Availability

The data that support this study are available from the corresponding author upon reasonable request.

References

1. Shi JL et al (2021) Wide Bandgap Oxide Semiconductors: from Materials Physics to Optoelectronic Devices. Adv Mater 50:2006230
2. Greiner TM et al (2013) Thin-film metal oxides in organic semiconductor devices: their electronic structures, work functions and interfaces. NPG Asia Mater 5:e55
3. Bronstein H et al (2020) The role of chemical design in the performance of organic semiconductors. Nat Rev Chem 4:66–77
4. Lüssem B et al (2013) Doping of organic semiconductors. Phys Status Solidi A 210:9–43

5. Nakamura S et al (1992) Hole Compensation Mechanism of p-Type GaN Films. Jpn J Appl Phys 31:1258
6. Park HC et al (2002) Origin of p-type doping difficulty in ZnO: The impurity perspective. Phys Rev B 66:073202
7. Elp VJ et al (1992) Electronic structure of Li-doped NiO. Phys Rev B 45:1612–1622
8. Wang ZW et al (2016) Recent Developments in p-Type Oxide Semiconductor Materials and Devices. Adv Mater 20:3831–3892
9. Mott FN (1949) The Basis of the Electron Theory of Metals, with Special Reference to the Transition Metals. *Proc. Phys. Soc. London, Sec. A* 62, 416
10. Hubbard J (1964) Electron correlations in narrow energy bands. II. The degenerate band case. *J. Proc. R. Soc. London, Sec. A* 277, 237
11. Fujimori A et al (1984) Valence-band photoemission and optical absorption in nickel compounds. Phys Rev B 30:957
12. Zaanen J et al (1985) Band Gaps and Electronic Structure of Transition-Metal Compounds. Phys Rev Lett 55:418
13. Hüfner S (1984) Bandstructure and atomic energy levels in Ce-Metal, NiO and NiS. Z Phys B: Condens Matter 58:1–6
14. Kelly PH (1963) Correlation Effects in Atoms. Phys Rev 131:684
15. Löwdin OP (1955) Quantum Theory of Many-Particle Systems. II. Study of the Ordinary Hartree-Fock Approximation. Phys Rev 97:1490
16. Thouless DJ (1961) The Quantum Mechanics of Many-Body Systems. Academic, New York
17. Hüfner S (2003) Photoelectron Spectroscopy: Principles and Applications, 3rd edn. Springer
18. Shen XZ et al (1990) Aspects of the correlation effects, antiferromagnetic order, and translational symmetry of the electronic structure of NiO and CoO. Phys Rev Lett 64:2442
19. Shen XZ (1991) Electronic structure of NiO: Correlation and band effects. Phys Rev B 44:3604
20. Mashford SB et al (2010) All-inorganic quantum-dot light-emitting devices formed via low-cost, wet-chemical processing. J Mater Chem 20:167–172
21. Bai S et al (2014) Low-Temperature Combustion-Synthesized Nickel Oxide Thin Films as Hole-Transport Interlayers for Solution Processed Optoelectronic Devices. Adv Energy Mater 4:1301460
22. You JB et al (2016) Improved air stability of perovskite solar cells via solution-processed metal oxide transport layers. Nat Nanotech 11:75–81
23. Jiang F et al (2015) Post-treatment-Free Solution-Processed Non-stoichiometric NiO_x Nanoparticles for Efficient Hole-Transport Layers of Organic Optoelectronic Devices. Adv Mater 18:2930–2937
24. Yu SQ et al (2023) Homogenized NiOx nanoparticles for improved hole transport in inverted perovskite solar cells. Science 6677:1399–1404
25. Li L et al (2022) Flexible all-perovskite tandem solar cells approaching 25% efficiency with molecule-bridged hole-selective contact. Nat Energy 7:708–717

26. Ballhausen CJ (1962) Introduction to Ligand Field Theory. McGraw-Hill, New York
27. Bishop DM, Klein DJ (2012) Group Theory and Chemistry. *Physics Today*, Vol. 28Dover Publications
28. Slater CJ, Koster FG (1954) Simplified LCAO method for the Periodic Potential Problem. Phys Rev 94:1498–1524
29. Hüfner S et al (1973) X-Ray Photoelectron Band Structure of Some Transition-Metal Compounds. Phys Rev B 8:4857
30. Hüfner S et al (1984) On the interpretation of valence band photoemission spectra of NiO. Solid State Commun 50:83–86
31. McKay MJ et al (1984) Structure of Valence and Conduction Levels in NiO. Phys Rev Lett 24:2343–2346
32. Hüfner S et al (1992) The optical gap of NiO. Z Phys B: Condens Matter 86:207–215
33. Kohn W (1957) Effective Mass Theory in Solids from a Many-Particle Standpoint. Phys Rev 105:509
34. Kim HJ et al (2014) High-Performance and Environmentally Stable Planar Heterojunction Perovskite Solar Cells Based on a Solution-Processed Copper-Doped Nickel Oxide Hole-Transporting Layer. Adv Mater 4:695–701
35. Wannier G (1937) Phys Rev 52:191
36. Labille J et al (2010) Stability of Nanoparticles in Water. Nanomedicine 5:985–998
37. Min F et al (2014) Hydration layers on clay mineral surfaces in aqueous solutions: a review. Arch Min Sci 2:489–500
38. Sun HY et al (2021) Influence of particle size on the aggregation behavior of nanoparticles: Role of structural hydration layer. J Environ Sci 103:33–42
39. Sun Q (2009) The Raman OH stretching bands of liquid water. *Vib*. Spectrosc. 2, *213–217*
40. Carey MD (1998) Measurement of the Raman spectrum of liquid water. J Chem Phys 108:2669–2675
41. Romanenko VA et al (2018) In Situ Raman Study of Liquid Water at High. Press Appl Spectrosc 6:847–852
42. Fafarman TA et al (2010) Decomposition of Vibrational Shifts of Nitriles into Electrostatic and Hydrogen-Bonding Effects. J Am Chem Soc 132:12811–12813
43. Kryachko SE (2002) Hydrogen Bonding between Phenol and Acetonitrile. J Phys Chem A 106:4267–4271
44. Ye JZ et al (2024) Extending the defect tolerance of halide perovskite nanocrystals to hot carrier cooling dynamics. Nat Common 15:8120
45. Cong MY et al (2020) Carrier Multiplication and Hot-Carrier Cooling Dynamics in Quantum-Confined $CsPbI_3$ Perovskite Nanocrystals. J Phys Chem Lett 5:1921–1926
46. Oyama M et al (2002) An Intermediate State of the Triphenylamine Cation Radical Revealed Using an Electron-Transfer Stopped-Flow Method. Electrochem Solid-State Lett 5:E1–E3

47. Goushi K et al (2012) Efficient organic light-emitting diodes through up-conversion from triplet to singlet excited states of exciplexes. Appl Phys Lett 101:023306
48. Lee J-H et al (2014) An exciplex forming host for highly efficient blue organic light emitting diodes with low driving voltage. Adv Funct Mater 25:361–366
49. Lin Y et al (2023) Highly efficient (EQE > 27%) Yellow OLEDs using spiro[fluorene-9,9-phenanthren-10-one]-carbazole-based donor–acceptor-donor host materials. J Mater Chem C 11:3101–3111
50. Tsang D et al (2016) Operational stability enhancement in organic light-emitting diodes with ultrathin Liq interlayers. Sci Rep 6:22463
51. Tu B et al (2019) Novel molecular doping mechanism for n-doping of SnO_2 via triphenylphosphine oxide and its effect on perovskite solar cells. Adv Mater 31:1805944
52. Kresse G et al (1996) Efficiency of ab-initio total energy calculations for metals and semiconductors using a plane-wave basis set. Comput Mater Sci 6:15–50
53. Kresse G et al (1996) Efficient iterative schemes for ab initio total-energy calculations using a plane-wave basis set. Phys Rev B 54:11169–11186
54. Perdew JP et al (1996) Generalized gradient approximation made simple. Phys Rev Lett 77:3865–3868

Figures

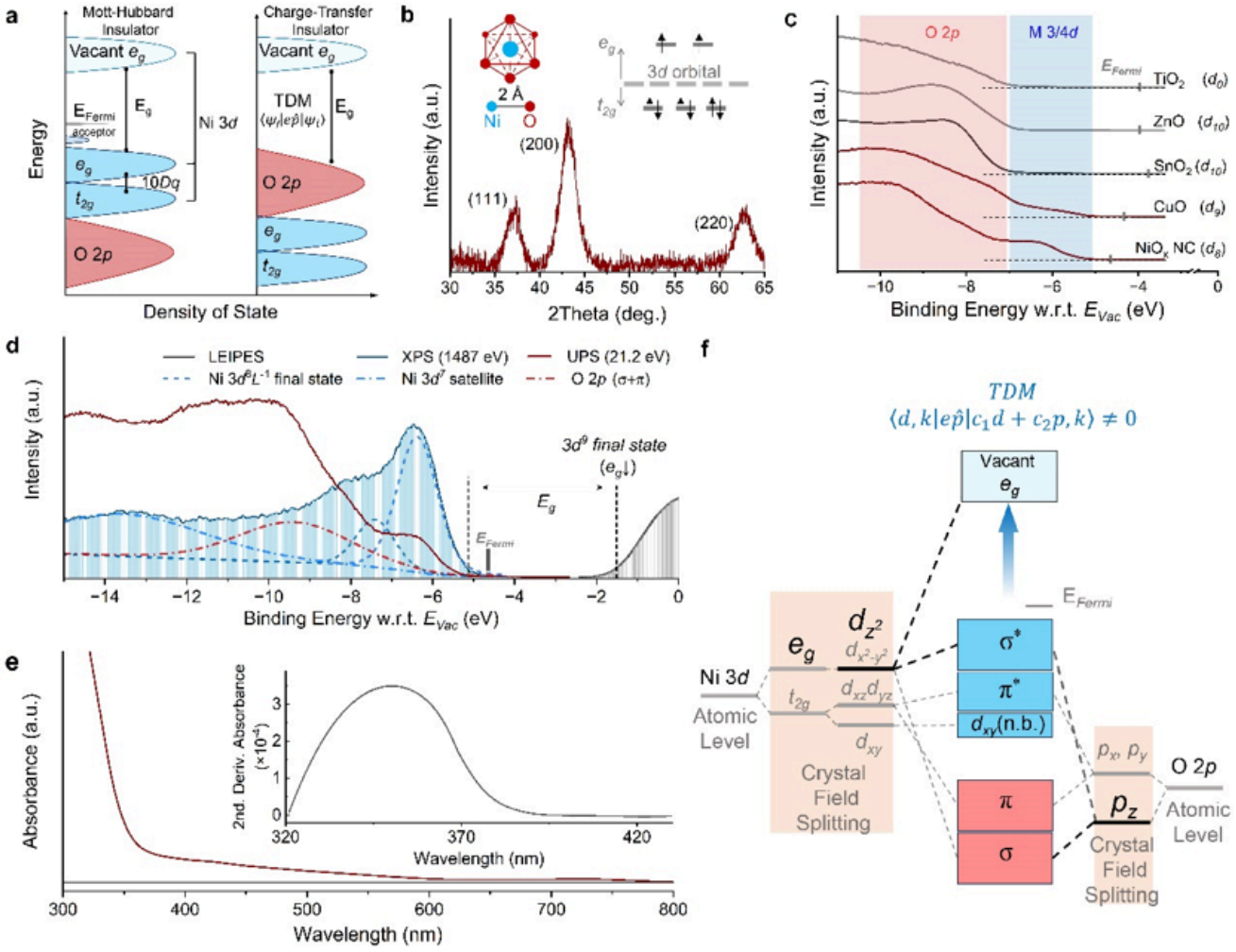


Figure 1

Band structure and interband transition dipole moment of NiO_x NC. a, Schematic band structures of the Mott-Hubbard insulator (left)[9,10] and the charge-transfer insulator (right)[11,12]. The Ψ_f, Ψ_i, e and $\hat{p}$ in the allowed transition dipole moment (TDM, Kane matrix element) denote the final state, initial state, polarization of the electric field and the momentum operator, respectively. **b**, XRD diffraction spectrum of NiO_x NC powder. The inset shows the crystal-field splitting of Ni 3*d* states into doubly degenerate e_g and triply degenerate t_{2g} levels[26]. **c**, UPS spectra of metal oxides featuring different *d* orbital occupancies. ***d***, UPS, valence-band XPS, and LEIPES spectra of NiO_x NCs. The electron-removal spectrum of the Ni 3*d* state is multiplet-structured, comprising the lowest-energy $3d^8$ final state ($3d^8L^{-1}$ in finite cluster theory, where *L* denotes O) and the 3*d* satellite (exited final state $3d^7$)[17], while the O 2*p* band in between integrates $p_{x,y}$ and p_z orbitals, forming *π*- and *σ*-bonds with Ni 3*d* orbitals[28]. **e**, UV-vis absorption spectrum of NiO_x NCs. The inset shows the second derivative of the absorption spectra. A weak absorption tail spanning the visible 370-600 nm is uniquely observed in these NiO_x NCs, accounting for their dark color. **f**, Orbital bonding scheme of NiO_x NC from atomic levels, crystal-field split levels to the

final interaction states in the Wannier representation[35]. The n.b. denotes a non-bonding state, and c_1 and c_2 in the matrix element represent the contribution ratios from various Wannier components.

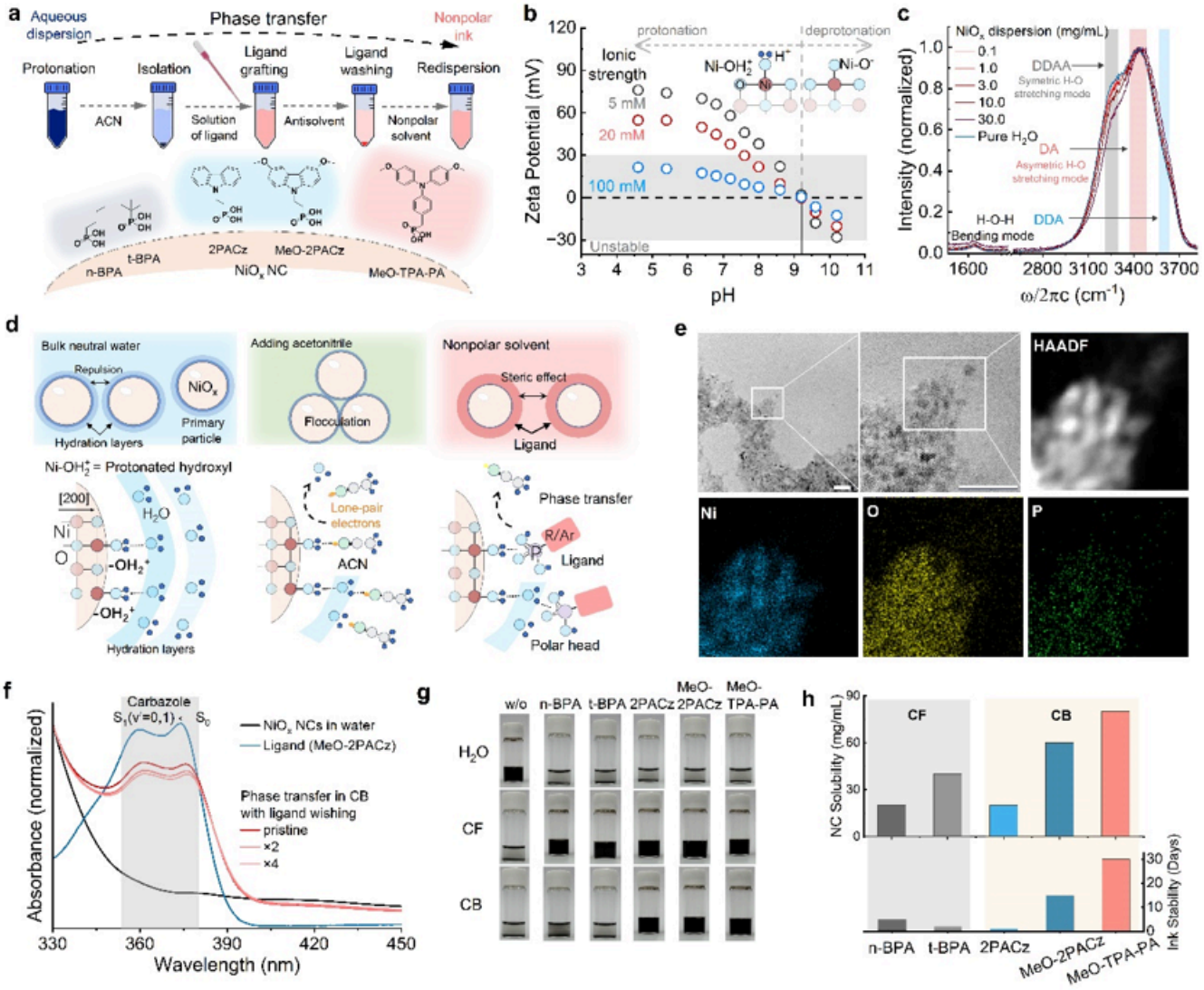


Figure 2

Phase transfer and colloidal ink properties of NiO_x NCs. a, Schematic illustration of the two-step ligand-exchange strategy for the functionalization and phase transfer of NiO_x NCs. The molecular structures of ligands are shown in the bottom half. **b**, The zeta potential of NiO_x NCs in aqueous dispersion measured over a range of pH values at different ionic strengths adjusted with KCl. **c**, Raman spectra of water in NiO_x NC aqueous dispersions over different concentrations. **d**, Diagram of the dispersibility and surface structural evolutions of NiO_x NCs at different stages of the phase-transfer process. **e**, TEM, high-angle annular dark field (HAADF) images, and the corresponding elemental maps of ligand-exchanged NiO_x NCs from nonpolar inks. **f**, UV-vis absorption spectra of the bare NiO_x NC aqueous suspension, MeO-2PACz ligands, and the ligand-exchanged NiO_x NC nonpolar inks under different rinse cycles. **g**,**h**, Colloidal dispersibility of various NiO_x NCs (g), and the corresponding solubility and ink stability of NiO_x

NCs varied by phosphonic acid ligands in different nonpolar media (h). The stability of the NiO_x NC inks was assessed by measuring the absorbance of samples stored for different periods.

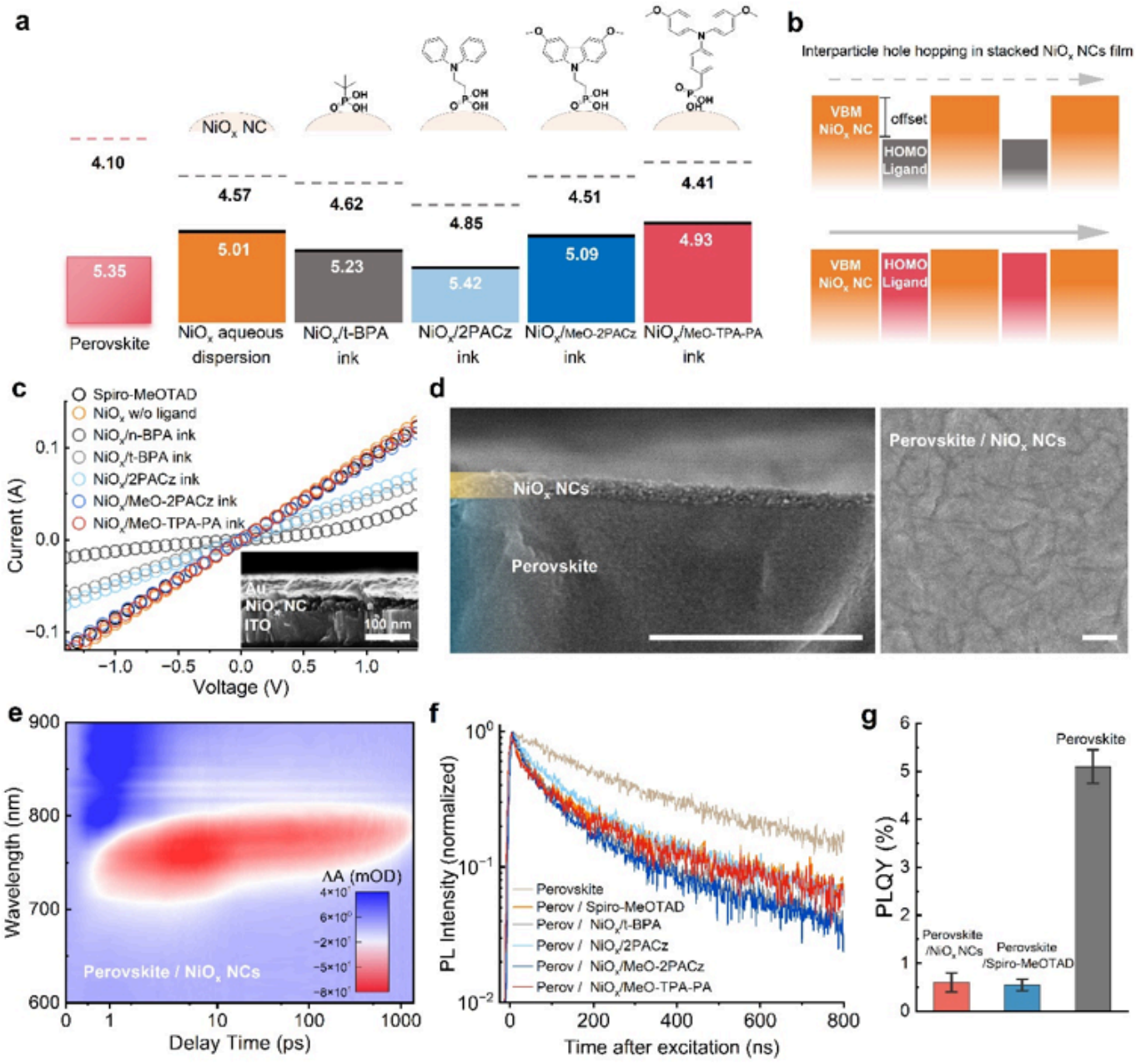


Figure 3

Electric properties of NiO_x NC films and the photogeneration dynamics of perovskite/ NiO_x NCs bilayers. a, Energy-level diagram of a variety of functional layers, including perovskite film, bare NiO_x NC film, and ligand-functionalized NiO_x NC films processed from nonpolar inks. Dash lines represent the Fermi level. **b**, Illustration of the energy level alignment and interparticle hole hopping in stacked NiO_x NC films with large (upper) and small (lower) energy level mismatches between NiO_x NC core and ligands. **c**, *I-V* curves of hole-only devices. The inset shows a cross-sectional SEM image of a hole-only device with

a 50-nm-thick NiO_x NC film. For the Spiro-OMeTAD device, a ~150-nm-thick film is used, matching the thickness of its photovoltaic devices. **d**, The cross-sectional and top-view SEM images of perovskite/ NiO_x NCs bilayers. The scale bar is 300 nm. **e**, Band-edge-excited TA map of perovskite/ NiO_x NCs bilayers using 700 nm pump. **f**, TRPL spectra of various perovskite/ HTL bilayers. **g**, PLQYs of bare perovskite and perovskite/ HTL bilayers (5 individual samples for each group with an excitation centered at 650 nm, 10 nm band pass).

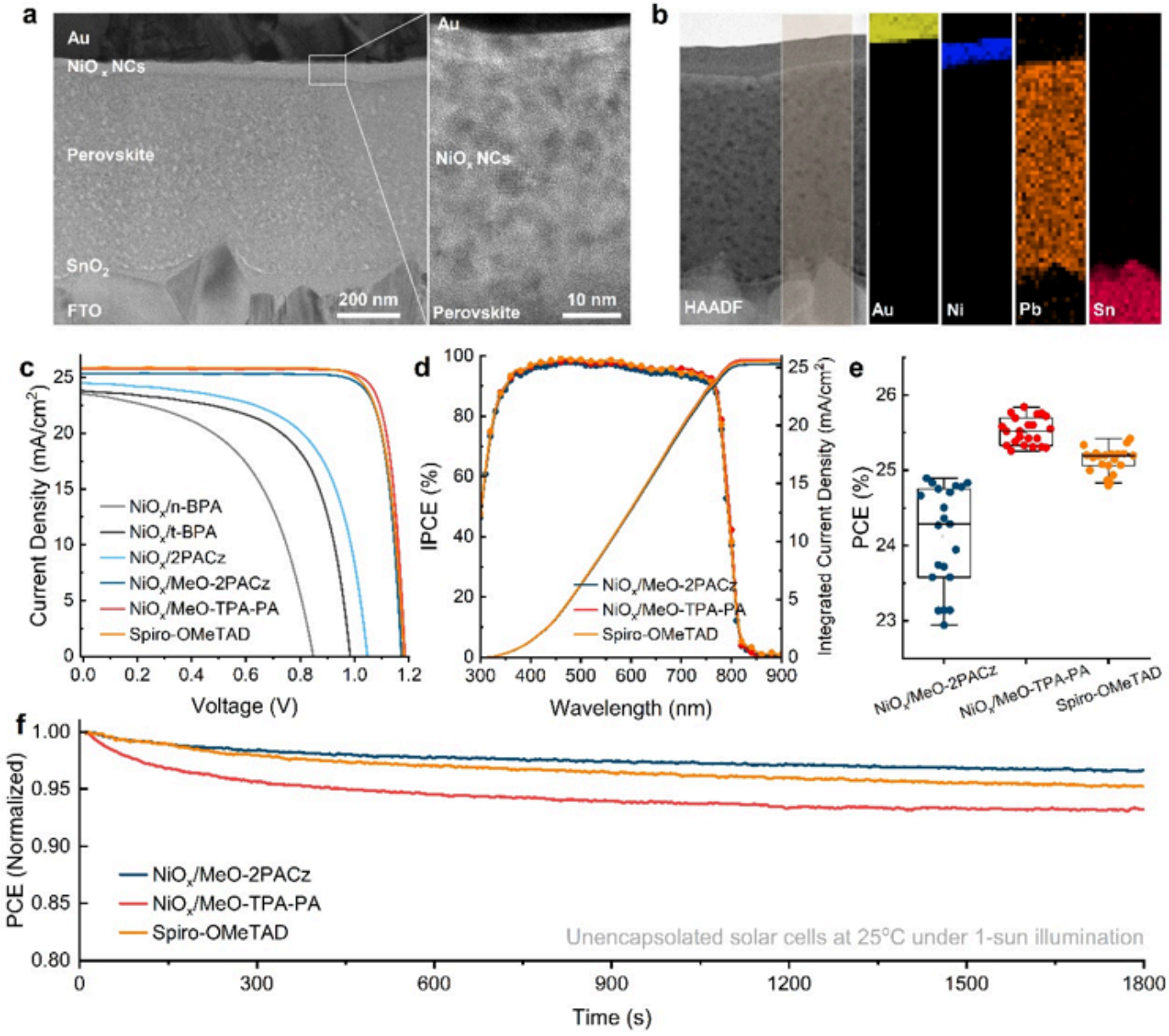


Figure 4

Photovoltaic performance of n-i-p perovskite solar cells employing nonpolar NiO_x NC inks. a,**b**, Cross-sectional TEM images (a), along with the HAADF image and corresponding elemental maps (b), of an n-i-p perovskite solar cell with NiO_x/ MeO-TPA-PA nanocrystals hole-transporting layer. **c**, Reverse-scan *J-V*

curves of n-i-p perovskite solar cells employing NiO_x NCs hole-transport layers with different phosphonic acid ligands. **d**, IPCE spectra of the champion NiO_x/MeO-2PACz, NiO_x/MeO-TPA-PA, and Spiro-OMeTAD devices (active area: 0.18 cm^2). **e**, Statistics of photovoltaic performance of NiO_x/MeO-2PACz, NiO_x/MeO-TPA-PA, and Spiro-OMeTAD devices (21 individual devices for each group). The bounds of the boxes are the 25th and 75th percentiles. **f**, The normalized MPP tracking of unencapsulated solar cells under continuous 1-sun illumination with temperature control, using an AM 1.5G solar simulator as the light source.

Supplementary Files

This is a list of supplementary files associated with this preprint. Click to download.

- SupportingInformation.docx